

# Accepted Manuscript

Reasonably retard O<sub>2</sub> consumption through a photoactivity conversion nanocomposite for oxygenated photodynamic therapy

Jin Zhang, Mengqing Xu, Yongli Mu, Jinjie Li, Mohamed F. Foda, Weiyun Zhang, Kai Han, Heyou Han

PII: S0142-9612(19)30411-9

DOI: <https://doi.org/10.1016/j.biomaterials.2019.119312>

Article Number: 119312

Reference: JBMT 119312

To appear in: *Biomaterials*

Received Date: 24 February 2019

Revised Date: 16 June 2019

Accepted Date: 26 June 2019

Please cite this article as: Zhang J, Xu M, Mu Y, Li J, Foda MF, Zhang W, Han K, Han H, Reasonably retard O<sub>2</sub> consumption through a photoactivity conversion nanocomposite for oxygenated photodynamic therapy, *Biomaterials* (2019), doi: <https://doi.org/10.1016/j.biomaterials.2019.119312>.

This is a PDF file of an unedited manuscript that has been accepted for publication. As a service to our customers we are providing this early version of the manuscript. The manuscript will undergo copyediting, typesetting, and review of the resulting proof before it is published in its final form. Please note that during the production process errors may be discovered which could affect the content, and all legal disclaimers that apply to the journal pertain.



# Reasonably retard O<sub>2</sub> consumption through a photoactivity conversion nanocomposite for oxygenated photodynamic therapy

Jin Zhang<sup>a</sup>, Mengqing Xu<sup>b</sup>, Yongli Mu<sup>b</sup>, Jinjie Li<sup>c</sup>, Mohamed F. Foda<sup>b,d</sup>, Weiyun Zhang<sup>a</sup>, Kai Han<sup>b</sup> and Heyou Han<sup>a,b,\*</sup>

<sup>a</sup> State Key Laboratory of Agricultural Microbiology, College of Life Science and Technology, College of Science, Huazhong Agricultural University, Wuhan 430070, Hubei, P. R. China

<sup>b</sup> State Key Laboratory of Agricultural Microbiology, College of Science, Huazhong Agricultural University, Wuhan 430070, Hubei, P. R. China

<sup>c</sup> State Key Laboratory of Agricultural Microbiology, College of Food Science and Technology, College of Science, Huazhong Agricultural University, Wuhan, Hubei 430070, People's Republic of China

<sup>d</sup> Department of Biochemistry, Faculty of Agriculture, Benha University, Moshtohor, Toukh 13736, Egypt

\*Corresponding author.

*E-mail address:* hyhan@mail.hzau.edu.

**Abstract**

Photodynamic therapy (PDT) brings excellent treatment outcome while also causing poor tumor microenvironment and prognosis due to the uncontrolled oxygen consumption. To solve this issue, a novel PDT strategy, oxygenated PDT (maintain the tumor oxygenation before and after PDT) was carried out by a tumor and apoptosis responsive photoactivity conversion nanocomposite (MPPa-DP). Under physiological conditions, this nanocomposite has a low photoactivity. While at H<sub>2</sub>O<sub>2</sub>-rich tumor microenvironment, the nanocomposite could react with overexpressed H<sub>2</sub>O<sub>2</sub> to produce O<sub>2</sub> and release high photoactivity chimeric peptide PPa-DP for oxygenated tumor and PDT. Importantly, when the PDT mediates cell apoptosis, the photoactivity of PPa-DP be effectively quenched and the O<sub>2</sub> consumption appeared retard, which avoided further consumption of residual O<sub>2</sub> on apoptotic cells. *In vitro* and *vivo* studies revealed that this nanocomposite could efficiently change photoactivity, reasonable control O<sub>2</sub> consumption and increase residual O<sub>2</sub> content of tumor after PDT.

*Keywords:* tumor and apoptosis responsive, photoactivity conversion, reasonable O<sub>2</sub> consumption, oxygenated photodynamic therapy

## 1. Introduction

Photodynamic therapy (PDT) as a potent therapy modality can efficiently convert dissolved oxygen ( $O_2$ ) into reactive oxygen species (ROS) to elicit cell death.[1, 2] However, the inherent hypoxia in tumor arising from the uncontrolled proliferation of cancer cells and distorted tumor blood vessels severely impairs ROS production and PDT treatment. Besides, the photoactivity of most photosensitizers (PS) during PDT are always ON. In order to maximize therapeutic effect, the persistent irradiation time and constantly activated PS would continuously convert  $O_2$  into  $^1O_2$  to oxidize the bio-substances of tumor cells containing apoptotic cells, which will further aggravate the extreme hypoxia of tumor[3-6] and induced the adverse Domino effects such as compromised therapy and poor prognosis.[7, 8]. To this end, many pioneering strategies have been developed to improve the intratumoral  $O_2$  level by delivered or in situ generation of  $O_2$ . [7, 9-14] However, they mainly highlight how to supply  $O_2$  to enhance the therapeutic effect. The side effect caused by  $O_2$  consumption in PDT is rarely considered. Although the tumor can be oxygenated to some extent, these  $O_2$  are still limited compared to the large amount of  $O_2$  loss in PDT, e. g. the low  $O_2$  loading efficiency and low  $H_2O_2$  content ( $< 100 \mu M$ ). [15, 16] Finally, the generated  $O_2$  in tumor would be rapidly depleted again. Therefore, how to prevent immoderate  $O_2$  consumption to improve the hypoxic tumor after PDT is of considerable importance. On the other hand, insufficient attention to controlling  $O_2$  consumption may be attributed to the challenge of fabricating an appropriate  $O_2$  consumption conversion system. Currently, there are many activateable PDT systems that realized photoactivity conversion to precisely treat tumor without off-target PS phototoxicity.[17, 18] These approaches mainly were “OFF-ON” mode that quenched PS by sophisticated synthetic method *in vitro* and activated based on various triggers

such as acidic,[19] redox,[20] protease,[21] H<sub>2</sub>S,[22] and hypoxia[23] in tumor site. However, the photoactivity “ON-OFF” system was hard to build due to the difficulty of performing complex chemical synthesis *in vivo* and rare triggers during PDT. More importantly, untimely intervention of O<sub>2</sub> consumption will severely impair the efficiency of PDT, resulting in the severe compromise of treatment. It can be imagined that if the tumor can be pre-oxygenated before PDT and a suitable trigger can inhibit the O<sub>2</sub> consumption reasonably to keep tumor oxygenation after PDT, the oxygenated PDT could be expected.

Keeping all these issues in mind, we prepared a caspase-3-triggered photoactivity conversion chimeric peptide to control the O<sub>2</sub> consumption in PDT based on aggregation-caused quenching (ACQ) theory[24, 25] due to the fact that PDT mainly mediates cell apoptosis by caspase-3/7 pathway.[26] The chimeric peptide was fabricated using i) a specified photosensitizer, pheophorbide-a (PPa), which has significant difference in photoactivity between monomeric and aggregated states[27, 28] for PDT and ii) a hydrophilic PEGylated Asp-Glu-Val-Asp (DEVD) peptide sequence which can be specifically cleaved by caspase-3 for changing the hydrophile-lipophilic-balance of PPa molecules. Under physiological conditions, the hydrophilic PEGylated DEVD polypeptide sequence could significantly increase the photoactivity of PPa molecules for facilitated the ROS generation.[29, 30] However, under enzyme caspase-3, the hydrophobic PPa molecules in PPa-DP underwent sharp aggregation due to detachment of the PEGylated DEVD fragment, resulting in a significant decrease in photoactivity. The change in photoactivity also changes the rate of O<sub>2</sub> consumption and realize control of O<sub>2</sub> consumption. To pre-oxygenated the tumor, we further adsorbed the chimeric peptide on high biocompatible MnO<sub>2</sub> nanosheets due to the high catalytic efficiency of MnO<sub>2</sub> with H<sub>2</sub>O<sub>2</sub>. As shown in

Scheme 1, the MnO<sub>2</sub> sheets could highly deliver PPa-DP into tumor cells and react quickly with intracellular H<sub>2</sub>O<sub>2</sub> to release O<sub>2</sub>, Mn<sup>2+</sup> and high photoactivity PPa-DP for PDT. Upon the apoptosis of cells, the activated caspase-3 in apoptotic cells would trigger quenching of photoactivity of PPa-DP and prevent the O<sub>2</sub> consumption. This apoptosis-triggered photoactivity conversion strategy was quite rational because i) there was no impair to treatment outcome, and ii) no additional oxygen is inappropriately acted on apoptotic tumor cells, which should maximize the O<sub>2</sub> content of the tumor after PDT.

## 2. Materials and methods

### 2.1. Reagents and materials

Rink Amide resin, N-fluorenyl-9-methoxycarbonyl (Fmoc)-protected L-amino acids, diisopropylethylamine (DIEA), o-benzotriazole-N,N,N',N'-tetramethyluroniumhexa fluorophosphates (HBTU) and piperidine were purchased from GL Biochem Ltd. (Shanghai, China). The Pheophorbide-a, PPa, was provided by Frontier Scientific (Logan, UT, USA). The caspase-3 was purchased from the R&D systems. Dulbecco's modified Eagle's medium (DMEM), trypsin, fetal bovine serum (FBS), MTT, and penicillinstreptomycin were purchased from GIBCO Invitrogen Corp. Tetramethylammonium hydroxide (TMA·OH), Manganese (II) chloride tetrahydrate (MnCl<sub>2</sub>·4H<sub>2</sub>O), and trifluoroacetic acid (TFA) were obtained from Shanghai Reagent Chemical Co. (China). 2',7'-dichlorofluorescein diacetate (DCFH-DA) were bought from Sigma-Aldrich. The hypoxia probe HP2-100Kit was acquired from Hypoxyprobe, Inc. The All other reagents and solvents were of analytical grade and used directly without further purification.

## 2.2. Preparation and characterization of MnO<sub>2</sub> nanosheets and PPa-DP

The MnO<sub>2</sub> nanosheets were prepared as previously reported.<sup>[31]</sup> Typically, 20 mL of a mixed aqueous solution of 0.6 M tetramethylammonium hydroxide and 3 wt % H<sub>2</sub>O<sub>2</sub> was added to 10 mL 0.3 M MnCl<sub>2</sub> solution within 15 s. When the two solutions were mixed, the mixture became dark brown immediately, indicating that Mn<sup>2+</sup> was oxidized to Mn<sup>4+</sup>. The resulting dark brown suspension was stirred vigorously overnight in the open air at room temperature. The as-prepared bulk manganese dioxide was centrifuged at 2000 rpm for 10 minutes and washed with copious amounts of distilled water and methanol, followed drying at 60 °C and storage for further use. The MnO<sub>2</sub> nanosheets were prepared by dispersing 10 mg bulk MnO<sub>2</sub> in 10 mL water, followed by ultrasonication for 10 h, centrifugation at the speed of 2000 rpm, and collecting the supernatant for further use. The concentration of as-prepared MnO<sub>2</sub> nanosheets was quantified through inductively coupled plasma optical emission spectrometry (Optima 8000 ICP-OES spectrometer, Perkin-Elmer) and diluted with ultrapure water to 1 g L<sup>-1</sup> for further use. The UV-vis absorption and XPS was conducted to characterize the successful formation of MnO<sub>2</sub> nanosheets.

PPa-DP was manually synthesized on Rink Amide resin (0.596 mmol g<sup>-1</sup>) via the conventional solid phase peptide synthesis procedure. After the resin was swollen in DMF for 1 h in nitrogen atmosphere, Fmoc group was deprotected using 20% piperidine in DMF at room temperature for 20 min. HBTU/DIPEA was used as coupling agents to sequentially couple amino acids to the N-terminus of peptide on resin. The PPa was introduced to peptide chain by coupling to ε-NH<sub>2</sub> of Lys using FMOC-Lys(Mtt)-OH as a linker. The PPa-DP was cleaved from the resin by a cleavage solution (TFA : TIS : H<sub>2</sub>O = 95 : 2.5 : 2.5) for 1.5 h. Then the crude product was prepared by precipitating the mixed solution in cold anhydrous diethyl ether and

drying under vacuum overnight. The crude was dissolved in distilled water and freeze-dried to obtain PPa-DP. The PPa-MP was prepared as a control using a similar method. The molecular weight was verified by electrospray ionization mass spectrometry (ESI-MS).

The UV-vis absorption of PPa-DP ( $50 \text{ mg L}^{-1}$ ) was measured using a UV-2450 UV-vis spectrophotometer. The hydrodynamic size was determined by Nano-ZS ZEN3600 (Malvern Instruments). The morphology of PPa-DP ( $50 \text{ mg L}^{-1}$ ) was observed with a transmission electron microscope (TEM, JEM-2100 microscope).

### 2.3. Preparation and characterization of MPPa-DP

The MPPa-DP were fabricated by mixing the PPa-DP with  $\text{MnO}_2$  under vigorous stirring for 2 h and further incubation for 6 h at room temperature. Then, the mixture was centrifuged through 30 kDa MWCO Amicon filters to remove the excessive PPa-DP. The MPPa-DP was obtained *via* re-dispersed the residue in water. The morphology, size and zeta potential of  $\text{MnO}_2$  ( $140 \text{ mg L}^{-1}$ ), MPPa-DP ( $240 \text{ mg L}^{-1}$ ) and MPPa-DP with  $\text{H}_2\text{O}_2$  was observed by TEM and Nano-ZS ZEN3600. The concentration of PPa-DP is  $100 \text{ mg L}^{-1}$ . Besides, the morphologies of  $\text{MnO}_2$  and MPPa-DP were further studied by scanning electron microscope (SEM, JSM-6390LV) and atomic force microscope (AFM, DIMultiMode8). The concentration of  $\text{MnO}_2$  is  $10 \text{ mg L}^{-1}$ . The fluorescence analysis of PPa-DP ( $30 \text{ mg L}^{-1}$ ), MPPa-DP ( $75 \text{ mg L}^{-1}$ ) and MPPa-DP with  $\text{H}_2\text{O}_2$  was performed with an RF-5301PC fluorospectrophotometer.

The degradation of  $\text{MnO}_2$  in  $\text{H}_2\text{O}_2$  was studied by optical imaging and ultraviolet spectrophotometer.  $100 \mu\text{L}$   $\text{MnO}_2$  and MPPa-DP (The concentration of  $\text{MnO}_2$  is  $300 \text{ mg L}^{-1}$ , pH 6.5) was added to ELISA plate strips with different concentrations of  $\text{H}_2\text{O}_2$ . After 15 min, the optical imaging and UV-Vis spectrum were obtained. The  $\text{O}_2$

generation by the reaction between MPPa-DP ( $200 \text{ mg L}^{-1} \text{ MnO}_2$ ) and  $\text{H}_2\text{O}_2/\text{H}^+$  (0.1 or 1 mM) was measured with an oxygen probe (JPBJ-608 portable Dissolved Oxygen Meters, Shanghai REX Instrument Factory).

#### 2.4. ROS detection

The ROS generation was measured using DCFH-DA as the sensor. Briefly, PPa-DP ( $30 \text{ mg L}^{-1}$ ) and DCFH-DA ( $250 \text{ }\mu\text{L}$ ,  $20 \text{ mg L}^{-1}$ ) were mixed with  $730 \text{ }\mu\text{L}$  PBS in a quartz cuvette, followed by light irradiation with 660 nm LED at preset time. The fluorescence spectrum from 500-550 nm was recorded at an excitation wavelength of 488 nm. PBS, Free PPa in 0.05% DMSO was used as control. The ROS generation ability was calculated with the formula:  $F_t/F_0$ .  $F_0$  is the initial fluorescence of samples without irradiation.  $F_t$  represents the fluorescence of samples with irradiation for a certain period of time.

#### 2.5. The effect of $\text{Mn}^{2+}$ on characterization of PPa-DP

Specifically,  $30 \text{ mg L}^{-1}$  PPa-DP solution ( $30 \text{ }\mu\text{L}$ ,  $1 \text{ g L}^{-1}$ ) was added into 1 mL of  $\text{MnCl}_2 \cdot 4\text{H}_2\text{O}$  solution with different concentrations of  $\text{Mn}^{2+}$ . After stirring for 1 h at room temperature, the effect of  $\text{Mn}^{2+}$  on PPa-DP was evaluated by UV-Vis \

pectrophotometer and fluorospectro photometer. The ROS generation of MnPPa-DP was measured by mixing PPa-DP ( $30 \text{ mg L}^{-1}$ ) with 30 equiv of  $\text{Mn}^{2+}$  via DCFH method.

#### 2.6. Caspase-3 mediated aggregation of PPa-DP

The caspase-3 induced aggregation of PPa molecules was investigated using TEM, UV-vis and fluorospectro spectrophotometer. For the UV-vis measurement, caspase-3 ( $20 \text{ }\mu\text{L}$ ,  $10 \text{ mg L}^{-1}$ ) was added to PPa-DP solution ( $200 \text{ }\mu\text{L}$ ,  $0.5 \text{ g L}^{-1}$ ), followed by immediate recording of the UV-vis absorption spectrum from 300 to 750 nm at preset time. For the fluorescence analysis, after mixing the caspase-3 solution and PPa-DP

solution, 10  $\mu\text{L}$  mixture was withdrawn at different time points and then diluted to 500  $\mu\text{L}$  for fluorescence analysis ( $\text{Ex} = 410 \text{ nm}$ ,  $\text{Em} = \text{band-pass } 600\text{-}700 \text{ nm}$ ). The aggregation behavior was further observed by TEM after incubation with caspase-3 over night. For comparison, the control group PPa-MP was tested under the same condition.

### *2.7. Caspase-3 mediated photoactive quenching of MPPa-DP and reduction of $\text{O}_2$ consumption*

To investigate the photoactivity change of PPa-DP, the generation of  $^1\text{O}_2$  was detected by the UV-vis absorbance spectrum using RNO plus histidine as the sensor. Briefly, RNO (50  $\mu\text{L}$ ,  $500 \times 10^{-6} \text{ M}$ ) and histidine (150  $\mu\text{L}$ ,  $60 \times 10^{-3} \text{ M}$ , as  $^1\text{O}_2$  trapping agent) were mixed to a total volume of 1 mL PBS, MPPa-DP, MnPPa-DP and PPa-DP with caspase-3 (pre-incubated for 1.5 h at  $37^\circ\text{C}$ ). The concentration of PPa-DP is  $30 \text{ mg L}^{-1}$ . Then, these samples were exposed to 660 nm LED and the UV-vis absorption change at 440 nm was evaluated at different time points. For  $\text{O}_2$  consumption assay, the sample, l-histidine ( $60 \times 10^{-3} \text{ M}$ ) and dissolved oxygen meter (JPBJ-608) were packed in a sealed glass bottle without residual air. When the dissolved  $\text{O}_2$  was stable, the samples were exposed to 660 nm LED, and the dissolved  $\text{O}_2$  was recorded at preset time. Finally, the  $\Delta\text{DO}$  was calculated as the initial value minus the measured value.

### *2.8. Cellular uptake and intracellular ROS generation study*

The cellular uptake of MPPa-DP nanoparticles was examined by confocal laser scanning microscopy (CLSM) and flow cytometry. For CLSM observation, the cells were seeded in a 35-mm confocal dish and incubated for 24 h. After washing three times with PBS, the cells were incubated with PPa-DP or MPPa-DP ( $30 \text{ mg L}^{-1}$ ) in a 1 mL DMEM for 0.5 and 2 h. After incubation, the cells were washed repeatedly with

PBS and the cell nuclei were stained with Hoechst 33342 for 15 min, followed by another wash with PBS for CLSM (Leica SP8, Germany). For flow cytometry, 4T1 cells were seeded in a 6-well plate and incubated for 24 h. Then the medium was replaced with new DMEM containing PPa-DP or MPPa-DP. After 0.5 and 2 h incubation, cells were washed, collected and resuspended in PBS. Finally, the samples were quantified *via* a FACS Calibur flow cytometer (BD Biosciences, USA).

The intracellular ROS generation was tested by CLSM, the 4T1 cells were seeded in confocal imaging chambers and incubated for 24 h, followed by addition of PPa-DP and MPPa-DP in DMEM at a concentration of  $10 \text{ mg L}^{-1}$  to the respective chambers. After 2 h incubation, the cells were washed three times and incubated with the ROS probe (DCFH-DA,  $10 \times 10^{-6} \text{ M}$ ). After 20 min incubation, the cells were washed again and exposed to 45 s light irradiation for CLSM. For quantification of intracellular ROS generation, the cells were digested by trypsin, collected, and resuspended in PBS for flow cytometry. Datas were analyzed using the Flowjo software.

### 2.9. Cell cytotoxicity assay

The cell cytotoxicity of PPa-DP or MPPa-DP was determined by MTT assay under  $\text{N}_2$  or  $\text{O}_2$  condition. Typically, 4T1 cells were seeded in 96-well plate and incubated for 24 h, followed by culture in the fresh medium with PPa-DP or MPPa-DP at various concentrations. After 2 h culture, the 96-well plates were placed in a transparent box ventilated with either  $\text{N}_2$  or  $\text{O}_2$  in advance and further incubated for 1 h, followed by irradiating the cells with 660 nm LED ( $10 \text{ mW cm}^{-2}$ ) for 45 s. After irradiation, the cells were incubated in fresh culture medium for another 24 h. The relative cell *viabilities* were measured by the standard MTT assay.

The dark cytotoxicity was analyzed by incubating 4T1 cells with different

concentrations of PPa-DP or MPPa-DP in 96-well plates. After incubation for 24 h, the standard MTT assay was conducted to measure the cell *viabilities*.

#### 2.10. *Caspase-3 mediated aggregation of MPPa-DP in cell*

First, the intracellular caspase-3 expression during PDT was examined by Western blotting analysis. After irradiation with a 660 nm laser ( $10 \text{ mW cm}^{-2}$ ) for a different period of time, the MPPa-DP-pretreated cells were lysed and collected immediately for WB analysis. The intracellular caspase-3 mediated aggregation of MPPa-DP was investigated *via* CLSM. Briefly, 4T1 cells were incubated with the MPPa-DP in a confocal dish for 2 h, followed by washing repeatedly in PBS and staining with Hoechst 33342 for 15 min. Next, cells were washed with PBS again and irradiated with 660 nm laser for 45 s. Finally, the cells were observed by CLSM at 0, 0.5 and 2 h post-irradiation.

#### 2.11. *Optical imaging, tissue distribution in vivo*

The optical imaging study was performed using a small animal imaging system. Typically, MPPa-DP (200  $\mu\text{g}$  in 100  $\mu\text{L}$  PBS, 4 mg/kg PPa per mouse) was injected into mice *via* tail vein. At preset time, the mice were anesthetized and imaged directly using the Maestro small animal imaging system (Cri inc.). At 24 h post-injection, the mice were sacrificed and the heart, liver, spleen, lung, kidney, and tumor were exfoliated and imaged for tissue distribution analysis.

#### 2.12. *Evaluation of tumor hypoxia, HIF-1 $\alpha$ and VEGF during PDT*

Female BALB/c mice bearing 4T1 tumor ( $\approx 200 \text{ mm}^3$ ) were administered intravenously with 100  $\mu\text{L}$  of MPPa-MP and MPPa-DP at the PPa-equivalent concentration of  $4 \text{ mg kg}^{-1}$ . At 24 h post-injection, the mice were irradiated with a 660 nm laser ( $10 \text{ mW cm}^{-2}$ ) for 0, 0.5, 1, 1.5 and 2 h, followed by the intraperitoneal injection of hypoxia-specific probe pimonidazole (hypoxyprom-1 plus kit,

Hypoxyprobe Inc.) at  $60 \text{ mg kg}^{-1}$  for covalent conjugation to thiolcontaining proteins in hypoxic tumor tissues. After 90 min, the tumors were excised and sectioned into  $10 \mu\text{m}$  thick slices with a cryostat, followed by incubation first with mouse anti-pimonidazole antibody and then with Alexa Fluor 488-conjugated goat anti-mouse secondary antibody according to the manufacturer's protocols. The hypoxia was assessed with a fluorescence microscope and the hypoxia area was analyzed with ImageJ software (Threshold value: 21). Then, we collected the tumors from MPPa-DP with 0 and 2 h irradiation, MPPa-MP with 2 h irradiation and PBS to further evaluate the expression of HIF-1 $\alpha$  and VEGF using the immunofluorescence and immunohistochemistry analysis. The slices were observed by a digital microscope (Leica QWin).

### 2.13. Antitumor therapy in vivo and histological analysis

Animal experiments were conducted in compliance with the criteria of The National Regulation of China.  $10^7$  of 4T1 tumor cells ( $100 \mu\text{L}$ ) was injected subcutaneously into the Female BALB/c mice. When the volume of 4T1 tumor xenograft growth was around  $100 \text{ mm}^3$ , the mice were randomly divided into 4 groups. PPa-DP, and MPPa-DP (dose of PPa =  $4 \text{ mg kg}^{-1}$ ,  $\text{MnO}_2$  =  $6 \text{ mg kg}^{-1}$ ) were intravenously injected into mice every two days. PBS and MPPa-DP without light irradiation were used as controls. At 24 h post-injection, the mice received 1 h light irradiation ( $660 \text{ nm}$ ,  $10 \text{ mW cm}^{-2}$ ). The tumor volume was measured per day and was calculated as follows:  $\text{volume} = (\text{tumor length}) \times (\text{tumor width})^2/2$ . At the end of treatment, the tumors in various groups were exfoliated and weighted for further evaluation of the antitumor effect. Relative tumor volumes were calculated as  $V/V_0$  ( $V_0$  is the tumor volume before treatment).

After treatment, the mice were sacrificed and the main organs and tumor were

exfoliated and fixed in 4% formalin, followed by embedding in paraffin for H&E staining. For the serum analysis, blood samples extracted from different groups were solidified and centrifuged at 3000 rpm for 15 min to obtain serum. Then, the TNF- $\alpha$  level in serum was detected using ELISA kits (Pub. No. MAN0017423).

#### 2.14. *The studies of MPP-DP mediated CDT*

The MPPa-DP was decomposed into  $\text{Mn}^{2+}$  under  $\text{H}_2\text{O}_2/\text{H}^+$  and further caused Fenton-like reaction with  $\text{H}_2\text{O}_2$  to generate  $\cdot\text{OH}$  for CDT was investigated by the degradation of methylene blue (MB) and cytotoxicity analysis. For the degradation of MB, the  $\text{MnO}_2$  ( $200 \text{ mg L}^{-1}$ , pretreated with  $\text{H}_2\text{O}_2/\text{H}^+$ ) was added to 50 mM  $\text{NaHCO}_3$  solution with different pHs of 6.5 and 7.4 containing  $10 \mu\text{g mL}^{-1}$  MB and 5 mM  $\text{H}_2\text{O}_2$ . Meanwhile, the group without  $\text{H}_2\text{O}_2$  and with pure  $\text{Mn}^{2+}$  ( $\text{MnCl}_2$ ) were used as negative and positive control, respectively. After 1 h at  $37^\circ\text{C}$ , the optical imaging of ELISA strips and UV-Vis adsorption spectra were recorded. For cytotoxicity assay, the 4T1 cells were seeded in 96-well plate and incubated for 24 h, and then the medium was replaced with different concentrations of MPPa-DP. After incubation for 24 or 48 h, the culture was extracted and 200  $\mu\text{L}$  new culture medium was added. After other 24 h, cell viability was evaluated by the MTT method. The PPa-DP and MPP-DP with Vitamin C (VC) was use as control.

#### 2.15. *Statistical analysis*

Statistical significance was analyzed by a three-sample Student's test. Statistical significance was inferred at a value of  $P < 0.05$ .

### 3. Results and discussion

### 3.1. Synthesis and characterization of MPPa-DP

The PPa-DP was synthesized through the standard Fmoc solid phase peptide synthesis (SPPS) method (Fig. S1) and the electrospray ionization mass spectrometry (ESI-MS) confirmed the validity of PPa-DP (Fig. S2). The MnO<sub>2</sub> sheets were prepared as previously reported<sup>[32]</sup>. The UV-vis adsorption spectrum (Fig. S3A), X-ray photoelectron spectrometer (XPS, Fig. S3B), SEM (Fig. S4) and AFM (Fig. S5A) indicated that the typical 2D MnO<sub>2</sub> sheet with a thickness of 2 nm was successfully prepared. Before loading the PPa-DP on MnO<sub>2</sub> sheets, we firstly verified that the pegylated DEVD peptide sequence could improve the water solubility and photochemical property of PPa (Fig. 1). Transmission electron microscopy (TEM) result showed that the amphiphilic PPa-DP could form well-dispersed and uniform spherical nanoparticles in PBS buffer (Fig. 1A). Dynamic light scattering (DLS) results further revealed that the corresponding hydrodynamic size was  $96.15 \pm 7.4$  nm (Fig. 1 B). There was discrepancy between DLS and TEM results due to the facts that i) the nanoparticles suffered from the shrinkage in vacuum state during TEM observation and ii) only high contrast part of PPa-DP could be extracted from TEM picture.<sup>[31, 33]</sup> The intermolecular interaction of PPa molecules in PPa-DP in various environmental conditions was also examined by the UV-vis spectroscopy. As shown in Fig. 1C, the Q<sub>y</sub>-band of free PPa in DMSO was a single peak at 677 nm, which is characteristic of the PPa monomer. However, the peak was redshifted to 685 nm in PBS, which is characteristic of the PPa dimer.<sup>[34]</sup> This difference was due to the  $\pi$ - $\pi$  stacking of PPa molecules in aqueous solution, and it can transform into monomers in DMSO. Note that the PPa-DP also displayed a sharp Q<sub>y</sub>-band at 677 nm in PBS, suggesting that the hydrophilic PEG and carboxyl groups in PPa-DP dramatically decreased the  $\pi$ - $\pi$  stacking among PPa molecules. The negligible  $\pi$ - $\pi$  stacking in this

nanoparticle would remarkably improve the bioactivity of PPa, especially in the generation efficacy of ROS.<sup>[27]</sup> Herein, we examined the ROS generation of PPa-DP using 2',7'-dichlorodihydrofluorescein diacetate (DCFH-DA) as a ROS sensor. In Fig. 1D, it can be seen that the free PPa and PBS displayed a low fluorescence increment with irradiation time prolonging. However, the fluorescence intensity increased quickly in PPa-DP under light irradiation, indicating that the pegylated DEVD peptide sequence can effectively improve the water solubility of the PPa and facilitate ROS generation.

The multifunctional nanocomposites (MPPa-DP) were fabricated as previously reported.<sup>[35]</sup> After mixing the PPa-DP with MnO<sub>2</sub> under vigorous stirring for 2 h and further incubation for 6 h, the AFM images (Fig. S5 A and B) showed a significant increase in the height of the MnO<sub>2</sub> after loading PPa-DP, indicating that the chimeric peptide was effectively adsorbed on MnO<sub>2</sub> sheet (the drug loading efficiency is 45%). Meanwhile, the appearance of LMCT absorption (Fig. S6) band peak at 415 nm in the optical absorption spectrum revealed the formation of Mn-N coordinate bonds between PPa-DP and MnO<sub>2</sub>,<sup>[36]</sup> which was consistent with previous reports.<sup>[35, 37]</sup> The optical images and DLS results (Fig. 2A and B) showed that the MnO<sub>2</sub> sheets and MPPa-DP could be uniformly dispersed in aqueous solution with an average hydrodynamic size of 137.9 and 212.5 nm, respectively. The zeta potential also changed from -26.9 mV to -21.2 mV (Fig. 2C). These dates implied the successful preparation of chimeric peptide -MnO<sub>2</sub> nanocomposites.

### 3.2. H<sub>2</sub>O<sub>2</sub>-triggered photoactivity enhancement and oxygen generation

Because MnO<sub>2</sub> can react with acid H<sub>2</sub>O<sub>2</sub> solution and be decomposed into water-soluble Mn<sup>2+</sup>.<sup>[37]</sup> Next, we demonstrated the reaction of MPPa-DP with H<sub>2</sub>O<sub>2</sub>. As the concentration of H<sub>2</sub>O<sub>2</sub> increases, the color and UV-vis absorption of MnO<sub>2</sub> at

pH 6.5 gradually disappeared (Fig. S7). The TEM results (Fig. 2A) also revealed that the  $\text{MnO}_2$  with sheet-like morphology disappeared under acidic  $\text{H}_2\text{O}_2$  and existed as a well-dispersed and uniform spherical nanoparticles. The corresponding size and zeta potential was 85.8 nm and -10.7 mV, which was similar to pure PPa-DP, indicating that the  $\text{MnO}_2$  was decomposed and the PPa-DP was released from MPPa-DP. Owing to  $\text{MnO}_2$  nanosheets have an intense and broad optical absorption spectrum, it can be used as an efficient fluorescence quencher, the fluorescence changes of MPPa-DP were also investigated. As shown in Fig. 2D, the fluorescence of PPa-DP decreased obviously after loading on  $\text{MnO}_2$  and recovered as expected under acidic  $\text{H}_2\text{O}_2$  solution, which further confirmed the decomposition of  $\text{MnO}_2$ . Meanwhile, we have further studied the effect of  $\text{Mn}^{2+}$  on PPa-DP by mixing  $\text{Mn}^{2+}$  with PPa-DP at different ratios. Only negligible change was observed in UV-vis adsorption spectrum of PPa-DP and the  $Q_y$ -band still remained as a single peak (Fig. S8A). Interestingly, although the molecular structure of PPa-DP unchanged, the fluorescence intensity appeared obvious decreased (Fig. S8B) after addition of  $\text{Mn}^{2+}$ , which was consistent with incomplete fluorescence recovery in Fig. 2D. A possible explanation is that the partial PPa molecules in PPa-DP might be coordinated with  $\text{Mn}^{2+}$ , giving a considerable enhancement to the deactivation and intersystem crossing of the excited singlet state.<sup>[35, 38, 39]</sup> The enhancement of intersystem crossing further increases the quantum yield of the triplet state and the ROS generation. Then, we evaluated the ROS generation of PPa-DP at same molar amount of  $\text{Mn}^{2+}$  as  $\text{MnO}_2$  (designed as MnPPa-DP). As expected, the  $\text{Mn}^{2+}$  obviously improved the ROS generation of PPa-DP, as evidenced by faster increment of fluorescence (Fig. 2E). In addition to  $\text{MnO}_2$ ,  $\text{H}_2\text{O}_2$  can also be decomposed into  $\text{O}_2$ . We also monitored the  $\text{O}_2$  generation using a dissolved oxygen (DO) meter. As shown in Fig. 2F, the DO in MPPa-DP with

H<sub>2</sub>O<sub>2</sub> increased remarkably within minutes while no change occurred in MPPa-DP or H<sub>2</sub>O<sub>2</sub> solution, suggesting that MPPa-DP could trigger rapid decomposition of H<sub>2</sub>O<sub>2</sub> to generate O<sub>2</sub>.

MnO<sub>2</sub> has been reported to facilitate drug internalization. The delivery efficacy of MPPa-DP was examined by confocal laser scanning microscopy (CLSM) and flow cytometry. Compared to the pure PPa-DP, a stronger red fluorescence was found in MPPa-DP at 0.5 h and 2 h (Fig. 3A). Flow cytometry (Fig. 3C) also showed a similar result, demonstrating the excellent delivery efficacy of MnO<sub>2</sub> sheets. The intracellular ROS levels were also examined using ROS probe DCFH-DA. A brighter green fluorescence in MPPa-DP (Fig. 3B and C) demonstrated that MPPa-DP could generate more intracellular ROS. Subsequently, we investigated the PDT efficiency of MPPa-DP against hypoxia by MTT assay under N<sub>2</sub> and O<sub>2</sub> conditions. Without light irradiation, both PPa-DP and MPPa-DP presented negligible cell dark-cytotoxicity (Fig. S9). Under light irradiation (10 mW cm<sup>-2</sup>) and O<sub>2</sub> conditions, both PPa-DP and MPPa-DP exhibited excellent phototoxicity to 4T1 cells (Fig. 3D). Meanwhile, the MPPa-DP had higher cell toxicity than PPa-DP, partly due to the efficient delivery efficacy and Mn<sup>2+</sup>-mediated enhancement of photoactivity. However, under N<sub>2</sub> atmosphere, the cell cytotoxicity of MPPa-DP and PPa-DP displayed great difference. MPPa-DP still maintained the excellent PDT efficacy as proved by the death of more than 50% cells at the PPa concentration of 15 μM. In sharp contrast, more than 85% cells in PPa-DP group survived under the same condition. All these results indicated that MPPa-DP could effectively improve the hypoxic environment of tumor and facilitate the PDT.

### 3.3. Caspase-3 induced reduction of photoactivity and oxygen consumption

Thereafter, we studied the aggregation behavior of PPa molecular mediated by

caspase-3 *in vitro* (Fig. 4A). TEM data showed that the size of nanocomposites significantly increased in TEM after treatment with caspase-3 (Fig. 4B). The Q<sub>y</sub>-band also became a broadened double peak at 667 nm and 683 nm as depicted in Fig. 4C. The time-dependent UV-vis spectrum from 600 nm to 700 nm (Fig. 4D) further revealed that the Q<sub>y</sub>-band gradually shifted from 667 nm to 683 nm, clearly indicating the aggregation of PPa molecules. Fluorescence analysis was conducted to further confirm this aggregation behavior due to the ACQ effect. After incubation with caspase-3, the fluorescence intensity (Fig. 4E) quickly dropped and was less than 50% within 30 min. The caspase-3 could effectively target the cleavage of the carboxylic terminal of PEGylated DEVD peptide sequence and induce the aggregation of hydrophobic PPa *via*  $\pi$ - $\pi$  stacking, which caused the red-shift of Q<sub>y</sub>-band and fluorescence quenching. The aggregation behavior would greatly impair the bioactivity of PPa, and the ROS production was detected again by using the well-established N, N-dimethyl-4-nitrosoaniline (RNO) photobleaching method. The <sup>1</sup>O<sub>2</sub> generation capacity of PBS, MPPa-DP, MnPPa-DP and MnPPa-DP with caspase-3 at the same PPa concentration was assessed by calculating the change value (- $\Delta A$ ) of the UV-vis absorption at 440 nm for RNO. As shown in Fig. 4F, a gradual increase of - $\Delta A$  implied that the MPPa-DP could generate <sup>1</sup>O<sub>2</sub> to oxidize RNO under irradiation. However, a faster increment of - $\Delta A$  in MnPPa-DP suggested the high photoactivity after decomposition of MnO<sub>2</sub> as demonstrated above. In sharp contrast, the increment of - $\Delta A$  was significantly retarded after incubation with caspase-3, implying the low photoactivity of PPa. The low photoactivity would reduce the conversion efficiency of <sup>3</sup>O<sub>2</sub> to <sup>1</sup>O<sub>2</sub>, and decrease O<sub>2</sub> consumption correspondingly. To confirm this, we tested the O<sub>2</sub> consumption of various samples by using a simple method. The sample, l-histidine ( $60 \times 10^{-3}$  M, as <sup>1</sup>O<sub>2</sub> trapping agent) and a dissolved oxygen meter were

packed in a sealed glass bottle without residual air in the dark. When the DO value reached a constant value, the glass bottles were exposed to laser irradiation and the DO value was recorded at preset time. As expected, after treatment with caspase-3, only a slight O<sub>2</sub> consumption was observed in Fig. 4G which agreed fairly well with the curve of <sup>1</sup>O<sub>2</sub> generation, suggesting the low O<sub>2</sub> consumption.

The caspase-3-mediated aggregation of MPPa-DP was also investigated in cells. As PDT mainly mediates cell apoptosis by caspase-3/7 pathway, we examined the expression of caspase-3 in 4T1 cells during PDT by Western Blot (WB) analysis. The 4T1 cells were seeded in a 10 cm<sup>2</sup> culture dish and incubated with MPPa-DP for 2 h. After removing the excess reagents, the cells were treated with laser irradiation or not and collecting the cells immediately for WB analysis. A identifiable black band representing the expression of caspase-3 was found in MPPa-DP with irradiation (Fig. 4H), whereas no or little caspase-3 expression was observed in control group and MPPa-DP without irradiation, suggesting that the PDT could effectively and rapidly induce the expression of caspase-3 in cells. Then, the intracellular aggregation was observed *via* CLSM analysis. Meanwhile, we synthesized a caspase-3-insensitive chimeric peptide ((PPa)KMGEDD-PEG<sub>8</sub>), designated as PPa-MP) as the control group. No difference occurred in UV-vis spectrum (Fig. S10A) and fluorescence intensity (Fig. S10B) before and after incubation with caspase-3 confirmed that the PPa-MP could not aggregate under caspase-3. For CLSM observation, the MPPa-DP and MPPa-MP was incubated with cells for 2 h, the cells were washed with PBS to remove the excess reagents and received 45 s light irradiation. At 0, 0.5 and 2 h post-irradiation, the intracellular fluorescence was observed by CLSM. As shown in Fig. 4I, a stronger intracellular red fluorescence representing MPPa-DP is clustered near the nuclear before light irradiation. However, the fluorescence was distributed

throughout the cell at 0.5 h post-irradiation, which might be due to the escape of MPPa-DP from endosome into the cytoplasm *via* photochemical internalization (PCI).<sup>[40]</sup> Interestingly, the red intracellular fluorescence became very weak in MPPa-DP at 2 h post-irradiation, whereas the fluorescence signal in MPPa-MP still remained strong. The CLSM images of MPPa-MP (Fig. S11) also showed that there was no obvious difference in the fluorescence intensity at 0.5 and 2 h post-irradiation, demonstrating that the aggregation could occur in cells. The caspase-3-mediated aggregation behavior can prevent the transformation of  $^3\text{O}_2$  to  $^1\text{O}_2$  to oxidize apoptotic cells, thereby precisely converting the rate of oxygen consumption after apoptosis and only targeting ROS to living cancer cells. Compared to the PDT systems with constantly active photosensitizer, the present system may ensure that the tumor maintains a high oxygen concentration.

#### 3.4. Elevation of oxygen and control of oxygen consumption *in vivo*

Based on the *in vitro* results, MPPa-DP was expected to boost  $\text{O}_2$  concentration in tumor tissues. Prior to studying the  $\text{O}_2$  content of tumor, we evaluated the *in vivo* bio-distribution of MPPa-DP using 4T1 tumor bearing nude mouse. Based on a small animal imaging system, we found that the MPPa-DP was accumulated quickly in tumor tissue within 2 h and reached its maximum at 4 h (Fig. 5A). The *ex vivo* fluorescence images of major organs and tumor (Fig. 5B) dissected from mice revealed that the tumor region still had high fluorescence signal at 24 h post-injection, indicating the high accumulation of MPPa-DP in tumor. Next, we performed PDT on mice with different treatment and evaluated tumor hypoxic by a hypoxia-specific probe pimonidazole. MPPa-MP and MPPa-DP were separately injected to mice intravenously. At 24 h post-injection, the tumors underwent different time light irradiation by a 660 nm LED ( $10 \text{ mW cm}^{-2}$ ). At the end of light irradiation,

pimonidazole was injected intraperitoneally into mice for imaging tumor hypoxia. Without laser irradiation, both MPPa-MP and MPPa-DP had lower expression of green fluorescence (Fig. 5C), evidencing that  $\text{MnO}_2$  could ameliorate tumor hypoxia due to the ability of  $\text{O}_2$  supply. As the extension of irradiation time, an increasing green fluorescence signal in all groups was observed. The quantitative results (Fig. 5D) also showed that the hypoxia positive area gradually increased. Obviously, the photosensitizers accumulated in tumor could transfer energy from light irradiation to the surrounding dissolved  $\text{O}_2$  and generate therapeutical ROS to oxidize the adjacent bio-substances, leading to the rapid elimination of  $\text{O}_2$ . Notably, the increment of hypoxia positive area in MPPa-MP was remarkably faster than that of MPPa-DP, as seen by the brighter green fluorescence, clearly demonstrating that the MPPa-DP with photoactivity conversion could improve the hypoxia microenvironment before and after PDT.

After 2 h irradiation, we further evaluated the HIF-1 $\alpha$  and VEGF expression using the immunofluorescence and immunohistochemistry analysis. The HIF-1 $\alpha$ , a key marker of hypoxia, and its downstream target, VEGF, is often associated with tumor growth and metastasis, which play a key role in progression of tumor. Without light irradiation, the PBS group exhibited strong red immunofluorescence as depicted in Fig. 5E due to the intrinsic tumor hypoxia. However, only an extremely weak red fluorescence was found in MPPa-DP without irradiation due to the production of  $\text{O}_2$ . After light irradiation, the MPPa-MP group had a strong red fluorescence indicated high expression of HIF-1 $\alpha$ . In contrast, the MPPa-dP had only a small amount of HIF-1 $\alpha$  expression. The VEGF expression also displayed similar result that only a little brown staining was found in MPPa-DP groups while a large number of brown staining appeared in the PBS and MPPa-MP group. The down-regulation of HIF-1 $\alpha$

and VEGF may be able to reduce the risk of tumor invasion and metastasis for better prognosis. [7, 41, 42]

### 3.5. Antitumor study in vivo

For antitumor effect, the 4T1 tumor-bearing mice were intravenously injected with PBS, MPPa-DP without irradiation, PPa-MP and MPPa-DP, respectively. At 24 h postinjection, the mice in treatment groups received irradiation (660 nm, 10 mW  $\text{cm}^{-2}$ ) for 1 h. The tumor volume of mice was recorded daily over treatment and the therapeutic effect was expressed by the relative tumor volume. As shown in Fig. 6A, the PBS and MPPa-DP without light irradiation afforded no antitumor performance. Besides, PPa-DP with light irradiation could inhibit tumor growth to some extent. By contrast, MPPa-DP exhibited a significant tumor inhibition effect. Meanwhile, the changes of body weight were monitored daily. Unobvious change of body weight had been observed in Fig. 6B. Additionally, the physiological morphology (Fig. S12) of various organs (heart, liver, spleen, lung, and kidney) in various groups was identified to be normal by H&E staining, with no pathological changes observed in the images of stained organ slices, suggesting the low systemic toxicity of MPPa-DP. At the end of treatment, the average tumor weight (Fig. 6C) and images of tumor tissues (Fig. 6D) were recorded. Significant difference that was similar to that of average tumor volume between MPPa-DP and other groups in tumor image and weight was found. The expression of TNF- $\alpha$  in murine serum and Hematoxylin and Eosin (H&E) staining of tumor slices further confirmed the therapeutical effect. A higher level of TNF- $\alpha$  and a more severe cell damage (the absence of blue dots) could be found in MPPa-DP with irradiation (Fig. S13 and Fig. 6E). All results suggested that MPPa-DP with self-supplied  $\text{O}_2$  and the photoactivity conversion not only greatly enhanced photodynamic efficiency, but also improved the poor tumor microenvironment in

PDT.

Besides, it is noteworthy that the MPPa-DP group also showed a discernible antitumor effect. This result might be attributed to  $Mn^{2+}$ -mediate chemodynamic therapy (CDT) described in previous literature.[43, 44] The decomposed  $Mn^{2+}$  in tumor acidic microenvironment could further react with  $H_2O_2$  to produce  $\cdot OH$  with the help of physiological  $HCO_3^-$  and lead to a discernible antitumor effect. In order to confirm it, the  $Mn^{2+}$ -mediate CDT was studied by the degradation of MB and cytotoxicity analysis. The Fig. S14A and B revealed that the pure and decomposed  $Mn^{2+}$  could rapidly produce hydroxyl radicals and completely degrade MB, a dye that can be degraded by hydroxyl radicals. The cell cytotoxic results (Fig. S14 C) indicated that the MPPa-DP could effectively cause the loss of cell viability after 48 h of incubation. Moreover, the cell damage could be alleviated by the addition of Vitamin C (VC, a ROS scavenger). Therefore, the excellent antitumor effect in MPPa-DP with light could also be attributed to the coexistence of CDT and PDT.

#### 4. Conclusions

In this study, we fabricated a photoactivity conversion  $MnO_2$ -chimeric peptide nanocomposite (MPPa-DP) to improve the  $O_2$  content of tumor before and after PDT. Firstly, low photoactive MPPa-DP could react with the endogenous  $H_2O_2$  in tumor to generate  $O_2$ ,  $Mn^{2+}$  and chimeric peptide PPa-DP for highly effective PDT. Secondly, upon the apoptosis of cells, the caspase-3 could specifically cleave the PEGylated DEVD peptide sequence, resulting in aggregation of PPa molecules. The aggregated PS with low photoactivity significantly reduced  $O_2$  consumption in subsequent PDT. Compared with the control group whose photoactivity was always on, MPPa-DP improved  $O_2$  content in tumor and downregulated the expression of HIF-1 $\alpha$  and VEGF after PDT, which should be a novel strategy to decrease the side effect caused

by uncontrollable elimination of O<sub>2</sub> during PDT.

### Acknowledgements

This work was supported by the Natural Science Foundation of China (21778020 and 31750110464) and Sci-tech Innovation Foundation of Huazhong Agriculture University (2662017PY042 and 2662018PY024). We thank Wuhan Institute of Virology, Chinese Academy of Sciences, for our *in vivo* fluorescence imaging work.

### References

- [1] Z. Zhou, J. Song, L. Nie, X. Chen, Reactive oxygen species generating systems meeting challenges of photodynamic cancer therapy, *Chem. Soc. Rev.* 45(23) (2016) 6597-6626.
- [2] Z.L. Yang, W. Tian, Q. Wang, Y. Zhao, Y.L. Zhang, Y. Tian, Y.X. Tang, S.J. Wang, Y. Liu, Q.Q. Ni, G.M. Lu, Z.G. Teng, L.J. Zhang, Oxygen-Evolving Mesoporous Organosilica Coated Prussian Blue Nanoplatfrom for Highly Efficient Photodynamic Therapy of Tumors, *Adv. Sci.* 5(5) (2018) 1700847.
- [3] A.L. Harris, Hypoxia--a key regulatory factor in tumour growth, *Nat. Rev. Cancer* 2(1) (2002) 38-47.
- [4] L. Cheng, C. Wang, L. Feng, K. Yang, Z. Liu, Functional Nanomaterials for Phototherapies of Cancer, *Chem. Rev.* 114(21) (2014) 10869-10939.
- [5] I. Lohse, C. Lourenco, E. Ibrahimov, M. Pintilie, M.S. Tsao, D.W. Hedley, Assessment of hypoxia in the stroma of patient-derived pancreatic tumor xenografts, *Cancers* 6(1) (2014) 459-71.
- [6] C. Qian, J. Yu, Y. Chen, Q. Hu, X. Xiao, W. Sun, C. Wang, P. Feng, Q.D. Shen, Z. Gu, Light-Activated Hypoxia-Responsive Nanocarriers for Enhanced Anticancer

- Therapy, *Adv. Mater.* 28(17) (2016) 3313-20.
- [7] X. Song, L. Feng, C. Liang, K. Yang, Z. Liu, Ultrasound Triggered Tumor Oxygenation with Oxygen-Shuttle Nanoperfluorocarbon to Overcome Hypoxia-Associated Resistance in Cancer Therapies, *Nano Lett.* 16(10) (2016) 6145-6153.
- [8] E.B. Rankin, A.J. Giaccia, Hypoxic control of metastasis, *Science* 352(6282) (2016) 175-180.
- [9] J. Bai, X. Jia, W. Zhen, W. Cheng, X. Jiang, A Facile Ion-Doping Strategy To Regulate Tumor Microenvironments for Enhanced Multimodal Tumor Theranostics, *J. Am. Chem. Soc.* 140(1) (2018) 106-109.
- [10] J. Kim, H.R. Cho, H. Jeon, D. Kim, C. Song, N. Lee, S.H. Choi, T. Hyeon, Continuous O<sub>2</sub>-Evolving MnFe<sub>2</sub>O<sub>4</sub> Nanoparticle-Anchored Mesoporous Silica Nanoparticles for Efficient Photodynamic Therapy in Hypoxic Cancer, *J. Am. Chem. Soc.* 139(32) (2017) 10992-10995.
- [11] H. Zhu, J. Li, X. Qi, P. Chen, K. Pu, Oxygenic Hybrid Semiconducting Nanoparticles for Enhanced Photodynamic Therapy, *Nano Lett.* 18(1) (2018) 586-594.
- [12] G. Yang, L. Xu, Y. Chao, J. Xu, X. Sun, Y. Wu, R. Peng, Z. Liu, Hollow MnO<sub>2</sub> as a tumor-microenvironment-responsive biodegradable nano-platform for combination therapy favoring antitumor immune responses, *Nat. Commun.* 8(1) (2017) 902.
- [13] H. Chen, J. Tian, W. He, Z. Guo, H<sub>2</sub>O<sub>2</sub>-activatable and O<sub>2</sub>-evolving nanoparticles for highly efficient and selective photodynamic therapy against hypoxic tumor cells, *J. Am. Chem. Soc.* 137(4) (2015) 1539-47.
- [14] Y. Cheng, H. Cheng, C. Jiang, X. Qiu, K. Wang, W. Huan, A. Yuan, J. Wu, Y. Hu,

Perfluorocarbon nanoparticles enhance reactive oxygen levels and tumour growth inhibition in photodynamic therapy, *Nat. Commun.* 6 (2015) 8785.

[15] B. Halliwell, M.V. Clement, L.H. Long, Hydrogen peroxide in the human body, *FEBS Lett.* 486(1) (2000) 10-13.

[16] D.W. Zheng, B. Li, C.X. Li, J.X. Fan, Q. Lei, C. Li, Z. Xu, X.Z. Zhang, Carbon-Dot-Decorated Carbon Nitride Nanoparticles for Enhanced Photodynamic Therapy against Hypoxic Tumor via Water Splitting, *ACS Nano* 10(9) (2016) 8715-22.

[17] X. Li, S. Kolemen, J. Yoon, E.U. Akkaya, Activatable Photosensitizers: Agents for Selective Photodynamic Therapy, *Adv. Funct. Mater.* 27(5) (2017) 1604053.

[18] B.M. Luby, C.D. Walsh, G. Zheng, Advanced Photosensitizer Activation Strategies for Smarter Photodynamic Therapy Beacons, *Angew. Chem., Int. Ed.* (2018).

[19] Y. Yuan, R.T. Kwok, B.Z. Tang, B. Liu, Smart Probe for Tracing Cancer Therapy: Selective Cancer Cell Detection, Image-Guided Ablation, and Prediction of Therapeutic Response In Situ, *Small* 11(36) (2015) 4682-90.

[20] H. Tong, Y. Chen, Z. Li, H. Li, T. Chen, Q. Jin, J. Ji, Glutathione Activatable Photosensitizer-Conjugated Pseudopolyrotaxane Nanocarriers for Photodynamic Theranostics, *Small* 12(45) (2016) 6223-6232.

[21] G. Zheng, J. Chen, K. Stefflova, M. Jarvi, H. Li, B.C. Wilson, Photodynamic molecular beacon as an activatable photosensitizer based on protease-controlled singlet oxygen quenching and activation, *Proc. Natl. Acad. Sci. U. S. A.* 104(21) (2007) 8989-94.

[22] Y. Ma, X. Li, A. Li, P. Yang, C. Zhang, B. Tang, H<sub>2</sub>S-Activable MOF Nanoparticle Photosensitizer for Effective Photodynamic Therapy against Cancer

with Controllable Singlet-Oxygen Release, *Angew. Chem., Int. Ed.* 56(44) (2017) 13752-13756.

[23] W. Piao, K. Hanaoka, T. Fujisawa, S. Takeuchi, T. Komatsu, T. Ueno, T. Terai, T. Tahara, T. Nagano, Y. Urano, Development of an Azo-Based Photosensitizer Activated under Mild Hypoxia for Photodynamic Therapy, *J. Am. Chem. Soc.* 139(39) (2017) 13713-13719.

[24] X. Xue, Y. Huang, R. Bo, B. Jia, H. Wu, Y. Yuan, Z. Wang, Z. Ma, D. Jing, X. Xu, W. Yu, T.Y. Lin, Y. Li, Trojan Horse nanotheranostics with dual transformability and multifunctionality for highly effective cancer treatment, *Nat. Commun.* 9(1) (2018) 3653.

[25] X. Li, S. Lee, J. Yoon, Supramolecular photosensitizers rejuvenate photodynamic therapy, *Chem. Soc. Rev.* 47(4) (2018) 1174-1188.

[26] A. Kulkarni, P. Rao, S. Natarajan, A. Goldman, V.S. Sabbiseti, Y. Khater, N. Korimerla, V. Chandrasekar, R.A. Mashelkar, S. Sengupta, Reporter nanoparticle that monitors its anticancer efficacy in real time, *Proc. Natl. Acad. Sci. USA* 113(15) (2016) E2104-E2113.

[27] W. Park, S.J. Park, S. Cho, H. Shin, Y.S. Jung, B. Lee, K. Na, D.H. Kim, Intermolecular Structural Change for Thermoswitchable Polymeric Photosensitizer, *J. Am. Chem. Soc.* 138(34) (2016) 10734-7.

[28] C. Tanielian, C. Wolff, M. Esch, Singlet oxygen production in water: Aggregation and charge-transfer effects, *J. Phys. Chem.* 100(16) (1996) 6555-6560.

[29] J. Zhang, Y.L. Mu, Z.Y. Ma, K. Han, H.Y. Han, Tumor-triggered transformation of chimeric peptide for dual-stage-amplified magnetic resonance imaging and precise photodynamic therapy, *Biomaterials* 182 (2018) 269-278.

[30] K. Han, W.-Y. Zhang, J. Zhang, Q. Lei, S.-B. Wang, J.-W. Liu, X.-Z. Zhang, H.-Y.

Han, Acidity-Triggered Tumor-Targeted Chimeric Peptide for Enhanced Intra-Nuclear Photodynamic Therapy, *Adv. Funct. Mater.* 26(24) (2016) 4351-4361.

[31] X. Dai, K. Han, Z. Ma, H. Han, A Chimeric Peptide Logic Gate for Orthogonal Stimuli-Triggered Precise Tumor Therapy, *Adv. Funct. Mater.* 28(47) (2018) 1804609.

[32] Y. Chen, D. Ye, M. Wu, H. Chen, L. Zhang, J. Shi, L. Wang, Break-up of two-dimensional MnO<sub>2</sub> nanosheets promotes ultrasensitive pH-triggered theranostics of cancer, *Adv. Mater.* 26(41) (2014) 7019-26.

[33] M.F. Foda, L. Huang, F. Shao, H.Y. Han, Biocompatible and highly luminescent near-infrared CuInS<sub>2</sub>/ZnS quantum dots embedded silica beads for cancer cell imaging, *ACS Appl Mater Interfaces* 6(3) (2014) 2011-7.

[34] I. Eichwurzel, H. Stiel, B. Roder, Photophysical studies of the pheophorbide a dimer, *J. Photochem. Photobiol. B* 54(2-3) (2000) 194-200.

[35] C. Chu, H. Lin, H. Liu, X. Wang, J. Wang, P. Zhang, H. Gao, C. Huang, Y. Zeng, Y. Tan, G. Liu, X. Chen, Tumor Microenvironment-Triggered Supramolecular System as an In Situ Nanotheranostic Generator for Cancer Phototherapy, *Adv. Mater.* 29(23) (2017).

[36] T. Takashima, K. Hashimoto, R. Nakamura, Inhibition of charge disproportionation of MnO<sub>2</sub> electrocatalysts for efficient water oxidation under neutral conditions, *J. Am. Chem. Soc.* 134(44) (2012) 18153-6.

[37] H. Fan, G. Yan, Z. Zhao, X. Hu, W. Zhang, H. Liu, X. Fu, T. Fu, X.B. Zhang, W. Tan, A Smart Photosensitizer-Manganese Dioxide Nanosystem for Enhanced Photodynamic Therapy by Reducing Glutathione Levels in Cancer Cells, *Angew. Chem., Int. Ed.* 55(18) (2016) 5477-82.

[38] Y. Yang, J. Liu, C. Liang, L. Feng, T. Fu, Z. Dong, Y. Chao, Y. Li, G. Lu, M. Chen, Z. Liu, Nanoscale Metal-Organic Particles with Rapid Clearance for Magnetic

- Resonance Imaging-Guided Photothermal Therapy, *ACS Nano* 10(2) (2016) 2774-81.
- [39] A. Harriman, Luminescence of porphyrins and metalloporphyrins. Part 1.—Zinc(II), nickel(II) and manganese(II) porphyrins, *Journal of the Chemical Society, Faraday Transactions 1: Physical Chemistry in Condensed Phases* 76(0) (1980) 1978.
- [40] H. Chen, L. Xiao, Y. Anraku, P. Mi, X. Liu, H. Cabral, A. Inoue, T. Nomoto, A. Kishimura, N. Nishiyama, K. Kataoka, Polyion complex vesicles for photoinduced intracellular delivery of amphiphilic photosensitizer, *J. Am. Chem. Soc.* 136(1) (2014) 157-63.
- [41] X.-S. Wang, J.-Y. Zeng, M.-K. Zhang, X. Zeng, X.-Z. Zhang, A Versatile Pt-Based Core-Shell Nanoplatfrom as a Nanofactory for Enhanced Tumor Therapy, *Adv. Funct. Mater.* 28(36) (2018).
- [42] W.L. Liu, T. Liu, M.Z. Zou, W.Y. Yu, C.X. Li, Z.Y. He, M.K. Zhang, M.D. Liu, Z.H. Li, J. Feng, X.Z. Zhang, Aggressive Man-Made Red Blood Cells for Hypoxia-Resistant Photodynamic Therapy, *Adv. Mater.* (2018) e1802006.
- [43] L.S. Lin, J. Song, L. Song, K. Ke, Y. Liu, Z. Zhou, Z. Shen, J. Li, Z. Yang, W. Tang, G. Niu, H.H. Yang, X. Chen, Simultaneous Fenton-like Ion Delivery and Glutathione Depletion by MnO<sub>2</sub>-Based Nanoagent to Enhance Chemodynamic Therapy, *Angew. Chem., Int. Ed.* 57(18) (2018) 4902-4906.
- [44] E. Ember, S. Rothbart, R. Puchta, R. van Eldik, Metal ion-catalyzed oxidative degradation of Orange II by H<sub>2</sub>O<sub>2</sub>. High catalytic activity of simple manganese salts, *New J. Chem.* 33(1) (2009) 34-49.

**Fig. captions**

**Scheme 1.** (A) The diagram shows adsorption, release and aggregation processes of PPa-DP. (B) Schematic illustration of photoactivity conversion nanocomposite (MPPa-DP) for oxygenated PDT. The chimeric peptides PPa-DP could be highly delivered into tumor cells by adsorbed on MnO<sub>2</sub> sheets. Then, the MnO<sub>2</sub> could react with the overexpressed H<sub>2</sub>O<sub>2</sub> to produce O<sub>2</sub> for pre-oxygenated tumor and release high photoactive PPa-DP for better PDT. Once the cell apoptosis, the high photoactive PPa-DP would rapidly quench its photoactivity and reduce the O<sub>2</sub> consumption. As a result, the low O<sub>2</sub> consumption could avoid excessive O<sub>2</sub> consumption, maintaining a high oxygen content after PDT.

**Fig. 1.** (A) TEM image, (B) hydrodynamic size, and (C) UV-vis spectrum of PPa-DP. (D) ROS generation of PPa-DP with different light irradiation time using DCFH-DA as sensor. Free PPa (in 0.5% DMSO) and PBS were used as controls.

**Fig. 2.** (A) the TEM images, (B) hydrodynamic size, (C) zeta potential and (D) fluorescence of MnO<sub>2</sub>, MPPa-DP, and MPPa-DP with H<sub>2</sub>O<sub>2</sub>. (E) The ROS generation of MnPPa-DP and PPa-DP. The DCFH-DA was used as sensor. (F) The oxygen generation curve of MPPa-DP at different H<sub>2</sub>O<sub>2</sub> concentration (0.1 mM or 1 mM). The H<sub>2</sub>O<sub>2</sub> and MPPa-DP alone were used as controls.

**Fig. 3.** (A) Confocal fluorescence images of 4T1 cells incubated with PPa-DP and MPPa-DP at different time points. The scale bar is 25  $\mu$ m. (B) Intracellular ROS generation of PPa-DP or MPPa-DP as detected by CLSM using ROS probe DCFH-DA. The scale bar is 75  $\mu$ m. (C) Corresponding flow

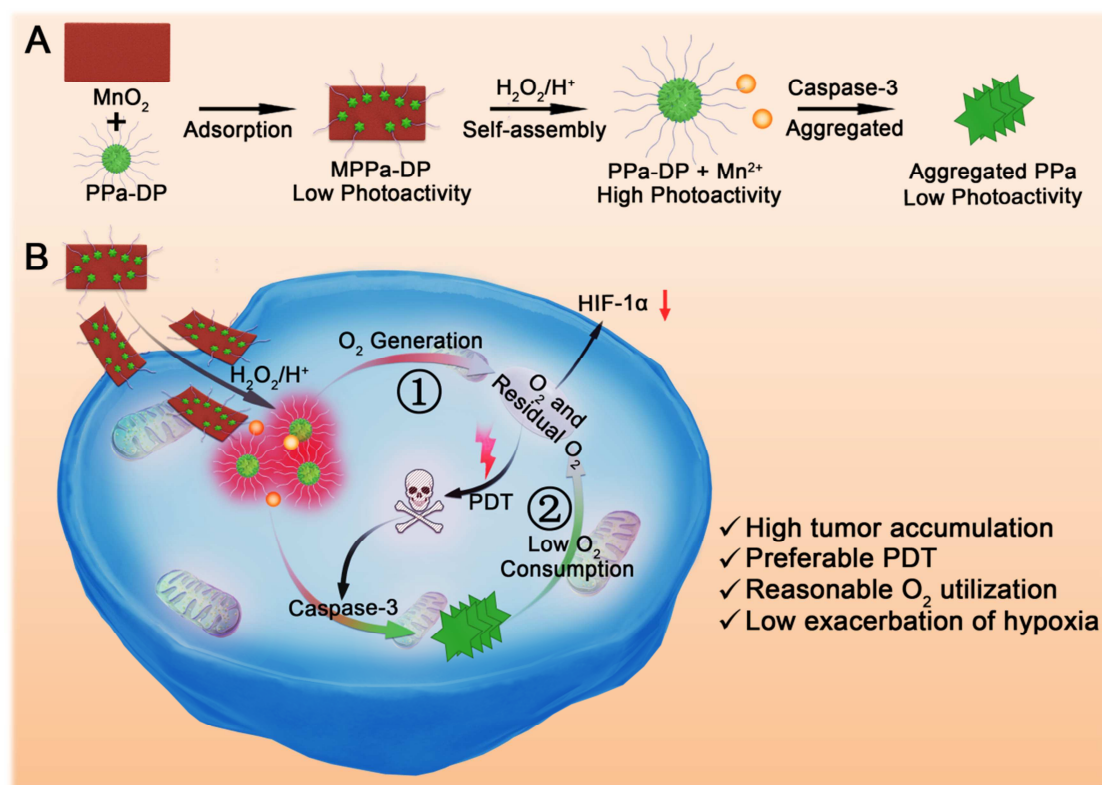
cytometry data. (D) *In vitro* PDT treatment of 4T1 cells by PPa-DP and MPPa-DP under light irradiation in N<sub>2</sub> or O<sub>2</sub> conditions.

**Fig. 4.** (A) Schematic illustration of the cleavage and aggregation of PPa-DP under caspase-3. (B) TEM image and (C) UV-vis adsorption spectra of PPa-DP after incubation with caspase-3. (D) The UV-vis adsorption spectra and (E) fluorescence spectra of PPa-DP upon incubation with caspase-3 for a different period of time. Inset: corresponding fluorescent images. (F) ROS generation efficiency of various groups as determined by the decrease of UV absorption at 440 nm under 660-nm irradiation using RNO as the sensor. The irradiation power is 10 mW cm<sup>-2</sup>. (G) The O<sub>2</sub> consumption ( $\Delta$ DO) of different treatments upon different irradiation times. (a) PBS; (b) MPPa-DP; (c) MnPPa-DP; (d) PPa-DP + caspase-3; (H) Western blots of caspase-3 in 4T1 cells treated with MPPa-DP. “L” represented 45 s light irradiation. (I) The intracellular fluorescence quenching at different time points after 45s laser irradiation as detected by CLSM. The scale bar is 25  $\mu$ m.

**Fig. 5.** *In vivo* fluorescence imaging. (A) *In vivo* fluorescence images of 4T1 tumor-bearing mice at different time points after *i.v.* injection of MPPa-DP. (B) MFI values and *ex vivo* fluorescence images of various organs and tumor tissue at 24 h post-injection. (C) The hypoxia of 4T1 tumors treated with MPPa-MP and MPPa-DP upon 660 nm irradiation (10 mW cm<sup>-2</sup>). Scale bar, 50  $\mu$ m. (D) Quantitative analysis of hypoxia-positive area from (A) was performed using ImageJ. (E) HIF-1 $\alpha$  and VEGF staining of 4T1 tumor tissues in MPPa-MP and

MPPa-DP with 2 h irradiation. The PBS and MPPa-DP without irradiation were used as control. Scale bar, 50  $\mu\text{m}$ .

**Fig. 6.** *In vivo* antitumor study. (A) Relative tumor volume after post-treatment; (B) relative body weight after post-treatment; (C) average tumor weight; and (D) tumor images at the 14th day. E) H&E staining of tumor tissues in different groups. The scale bar is 50  $\mu\text{m}$ . Asterisks (\*) represent the statistical significance: \* $p < 0.05$ , \*\* $p < 0.01$ , \*\*\* $p < 0.001$ .



**Scheme 1.** (A) The diagram shows adsorption, release and aggregation processes of PPa-DP. (B) Schematic illustration of photoactivity conversion nanocomposite (MPPa-DP) for oxygenated PDT. The chimeric peptides PPa-DP could be highly delivered into tumor cells by absorbed on MnO<sub>2</sub> sheets. Then, the MnO<sub>2</sub> could react with the overexpressed H<sub>2</sub>O<sub>2</sub> to produce O<sub>2</sub> for pre-oxygenated tumor and release high photoactive PPa-DP for better PDT. Once the cell apoptosis, the high photoactive PPa-DP would rapidly quench its photoactivity and reduce the O<sub>2</sub> consumption. As a result, the low O<sub>2</sub> consumption could avoid excessive O<sub>2</sub> consumption, maintaining a high oxygen content after PDT.

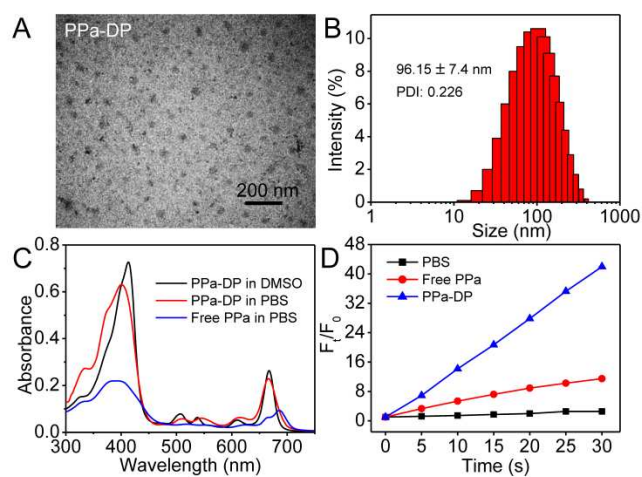


**Fig. 1.** (A) TEM image, (B) hydrodynamic size, and (C) UV-vis spectrum of PPa-DP. (D) ROS generation of PPa-DP with different light irradiation time using DCFH-DA as sensor. Free PPa (in 0.5% DMSO) and PBS were used as controls.

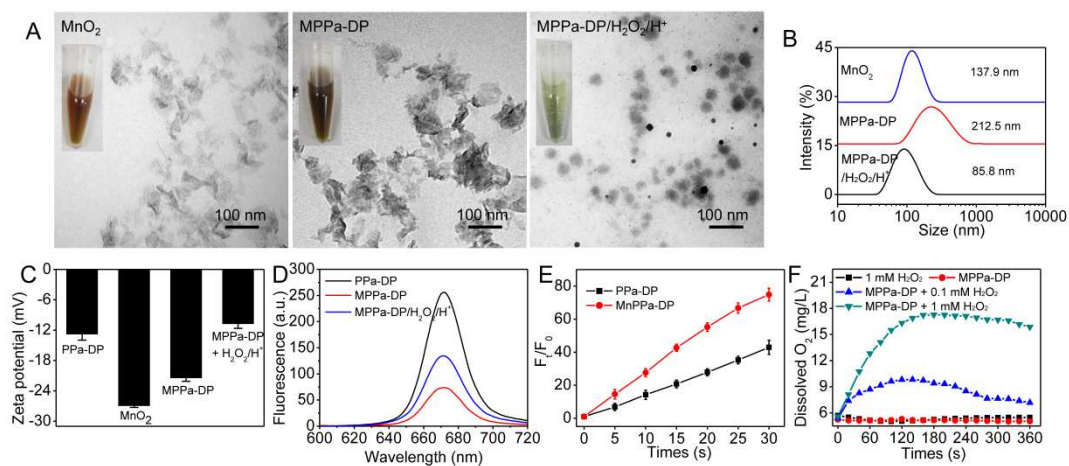


**Fig. 2.** (A) the TEM images, (B) hydrodynamic size, (C) zeta potential and (D) fluorescence of MnO<sub>2</sub>, MPPa-DP, and MPPa-DP with H<sub>2</sub>O<sub>2</sub>. (E) The ROS generation of MnPPa-DP and PPa-DP. The DCFH-DA was used as sensor. (F) The oxygen generation curve of MPPa-DP at different H<sub>2</sub>O<sub>2</sub> concentration (0.1 mM or 1 mM). The H<sub>2</sub>O<sub>2</sub> and MPPa-DP alone were used as controls.

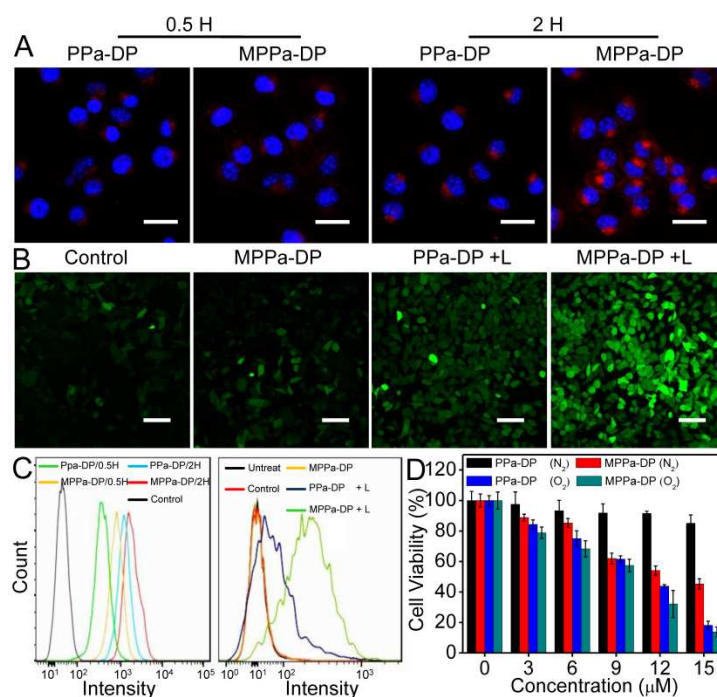


**Fig. 3.** (A) Confocal fluorescence images of 4T1 cells incubated with PPa-DP and MPPa-DP at different time points. The scale bar is 25  $\mu\text{m}$ . (B) Intracellular ROS generation of PPa-DP or MPPa-DP as detected by CLSM using ROS probe DCFH-DA. The scale bar is 75  $\mu\text{m}$ . (C) Corresponding flow cytometry data. (D) *In vitro* PDT treatment of 4T1 cells by PPa-DP and MPPa-DP under light irradiation in  $\text{N}_2$  or  $\text{O}_2$  conditions.

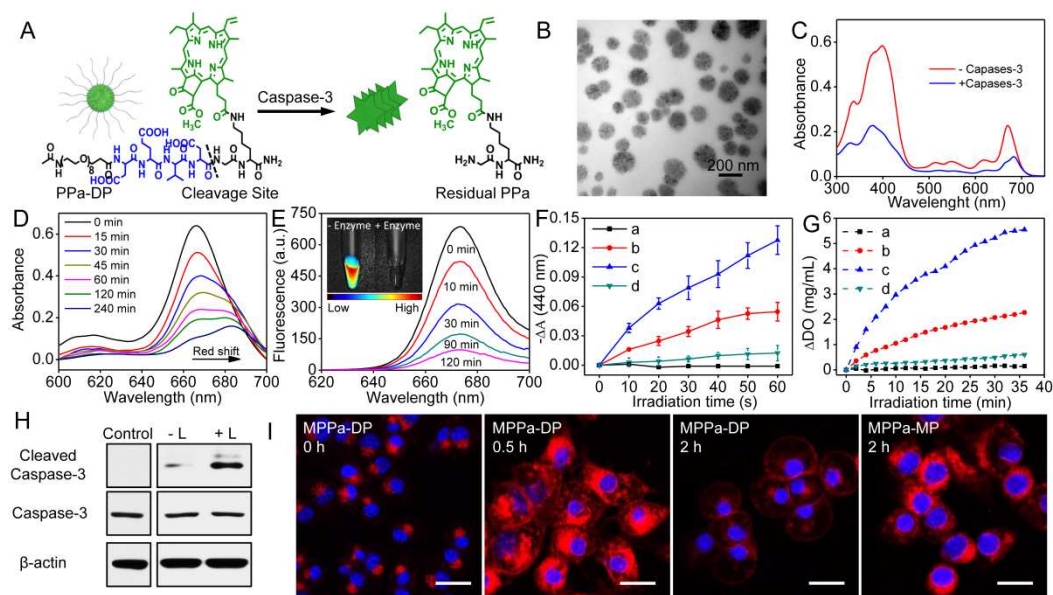


**Fig. 4.** (A) Schematic illustration of the cleavage and aggregation of PPa-DP under caspase-3. (B) TEM image and (C) UV-vis adsorption spectra of PPa-DP after incubation with caspase-3. (D) The UV-vis adsorption spectra and (E) fluorescence spectra of PPa-DP upon incubation with caspase-3 for a different period of time. Inset: corresponding fluorescent images. (F) ROS generation efficiency of various groups as determined by the decrease of UV absorption at 440 nm under 660-nm irradiation using RNO as the sensor. The irradiation power is  $10 \text{ mW cm}^{-2}$ . (G) The  $\text{O}_2$  consumption ( $\Delta\text{DO}$ ) of different treatments upon different irradiation times. (a) PBS; (b) MPPa-DP; (c) MnPPa-DP; (d) PPa-DP + caspase-3; (H) Western blots of caspase-3 in 4T1 cells treated with MPPa-DP. 4T1 cells without any treatment were used as control. “L” represented 45 s light irradiation. (I) The intracellular fluorescence quenching at different time points after 45s laser irradiation as detected by CLSM. The scale bar is  $25 \mu\text{m}$ .

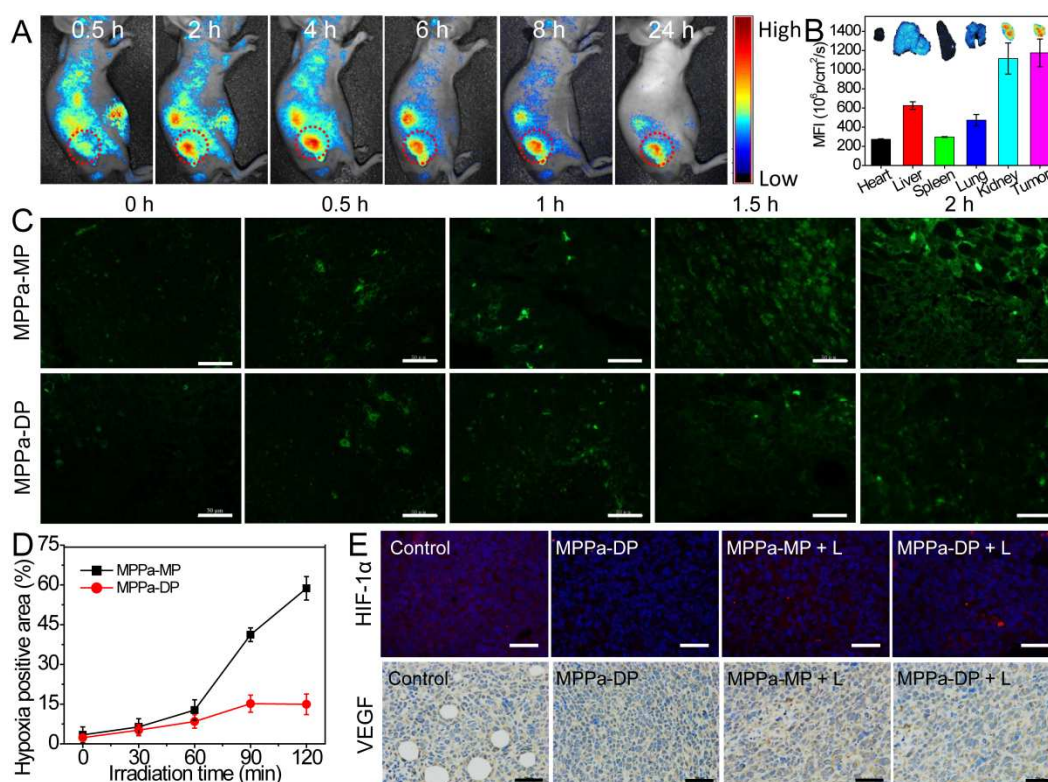


**Fig. 5.** *In vivo* fluorescence imaging. (A) *In vivo* fluorescence images of 4T1 tumor-bearing mice at different time points after *i.v.* injection of MPPa-DP. (B) MFI values and *ex vivo* fluorescence images of various organs and tumor tissue at 24 h post-injection. (C) The hypoxia of 4T1 tumors treated with MPPa-MP and MPPa-DP upon 660 nm irradiation (10 mW cm<sup>-2</sup>). Scale bar, 50 μm. (D) Quantitative analysis of hypoxia-positive area from (A) was performed using ImageJ. (E) HIF-1α and VEGF staining of 4T1 tumor tissues in MPPa-MP and MPPa-DP with 2 h irradiation. The PBS and MPPa-DP without irradiation were used as control. Scale bar, 50 μm.

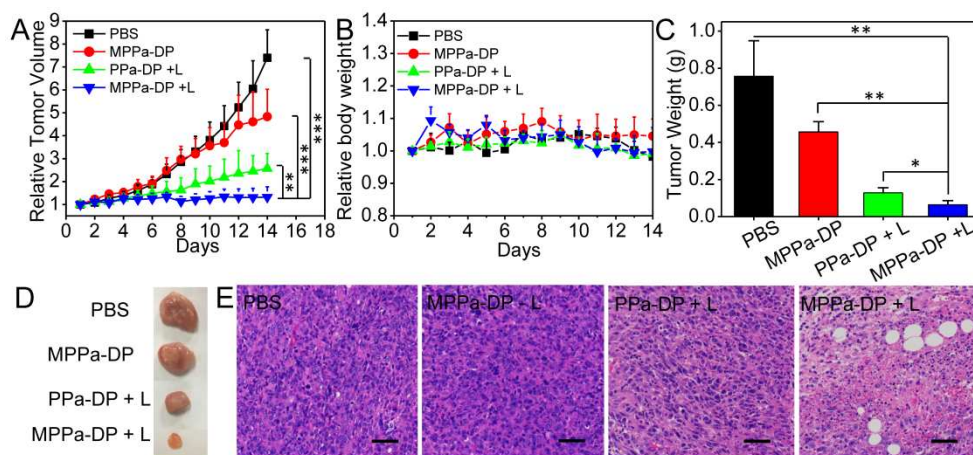


**Fig. 6.** *In vivo* antitumor study. (A) Relative tumor volume after post-treatment; (B) relative body weight after post-treatment; (C) average tumor weight; and (D) tumor images at the 14th day. E) H&E staining of tumor tissues in different groups. The scale bar is 50  $\mu$ m. Asterisks (\*) represent the statistical significance: \* $p < 0.05$ , \*\* $p < 0.01$ , \*\*\* $p < 0.001$ .